In Situ Observation of Cuprous Oxide Film Formation by Second Harmonic Generation

A Thesis Presented to the Faculty of the Department of Chemistry at the University of Houston

In Partial Fulfillment of the Requirement for the Degree of Master of Science

Submitted by

Michael Anthony Donovan

December 2013

In Situ Observation of Cuprous Oxide Film Formation by Second Harmonic Generation

---

Michael Anthony Donovan

APPROVED:

Dr. Steve Baldelli, Chairman

Dr. Vassiliy Lubchenko

Dr. Jeremy May

Dr. Shoujun Xu

Dr. Junrong Zheng

Dean, College of Natural Sciences and Mathematics

Acknowledgements

This thesis is the result of collaboration with many different members of Dr. Steve Baldelli's group, so in my opinion an acknowledgement is due. First of all, I'd like to thank Dr. Baldelli for allowing me to learn the ropes (and burns) of the Ti:Sapphire oscillator. I can never be grateful enough for this, and I feel that in this regard, my knowledge has increased exponentially since I arrived in the group. Ming Fang dedicated a lot of time to help in the initial sample preparation, and I am greatly appreciative. I am also indebted to Dien Ngo for giving me a great deal of laser time in which to perform these experiments. Thanks also go out to Jack Jacob and Quan Vo for assisting with the SFG experiments. Additionally, I would like to acknowledge other members, Siyun, Zlata, Chariz, Joon Hee, Greggy, Immee, and Xiaojun.

I am also indebted to my father for providing support throughout this experience, and additionally, I could have never completed this thesis if it wasn't for my one true love, yerba mate. Aside from the tea, I wish to acknowledge my mother and sisters, and last but not least, Turkey.

In Situ Observation of Cuprous Oxide Film Formation by Second Harmonic Generation

An Abstract of a Thesis Presented to the Faculty of the Department of Chemistry at the University of Houston

In Partial Fulfillment of the Requirement for the Degree of Master of Science

Submitted by

Michael Anthony Donovan

December 2013

ABSTRACT

In situ kinetic experiments utilizing surface specific second harmonic generation are used to observe the kinetics of oxide formation from polished Cu samples treated with amidosulfonic acid under dry air and humid air. The second harmonic signal is observed to decrease upon initial exposure to dry air followed by an increase in signal after 50 minutes of exposure. This is indicative of chemisorption of O_2 followed by formation of another monolayer of Cu_2O. Under humid conditions, the second harmonic signal increases immediately upon exposure to air. An aqueous adlayer accelerates the rate of Cu_2O formation. Finally, the kinetics of oxide formation are measured using Second Harmonic Generation on an octadecanethiol (ODT) coated Cu sample. ODT is observed to slow the growth in second harmonic signal. ODT is thus observed to slow the rate of Cu_2O formation.

Contents

Chapter 1: Introduction

Copper is a metal of industrial and commercial importance utilized for its excellent thermal and electrical properties. Its excellent properties have been known since the Bronze Age, and it is very easily molded. Copper is subject to atmospheric corrosion, and the metal is generally found in nature with a native oxide film Cu_2O chemisorbed to the substrate. Atmospheric corrosion, in general, is a complicated problem in surface science. Interactions can occur between the three different interfaces present in the system: the metal substrate, the physisorbed aqueous adlayer, and the gaseous environment.[1] Cuprous oxide film formation can be accelerated by the formation of an aqueous adlayer, and many studies have shown this. The influence of humidity can have profound effects on the formation of an oxide film. Briefly, it is useful to introduce water's interaction with metallic substrates.

Theoretical models suggest that water bonds to chemical surfaces via the oxygen atom, and that the bond energy to the surface is on the order of 40 – 65 kJ/mol.[2] This suggests weak chemisorption and possible physisorption to the metal surface, and water also forms a hydrogen bond network with the other water molecules at the surface.[2] The aqueous adlayer as such can affect oxide film formation at the copper surface, and basic IRAS and QCM studies have followed the in situ kinetics of oxide formation in the presence of humidity.[3,4] **Figure 1.1** shows the results of an in situ measurement of Cu_2O film formation. In this measurement, the sample was exposed to humidified air with a relative humidity of 80%, and intermittently, the sample was exposed to dry air. The

signal from both IRAS and QCM is observed to grow logarithmically over the course of the experiment, and as shown by the periods of dry air exposure, the growth in signal can be attributed to both oxide film formation and growth of the aqueous adlayer.[3]

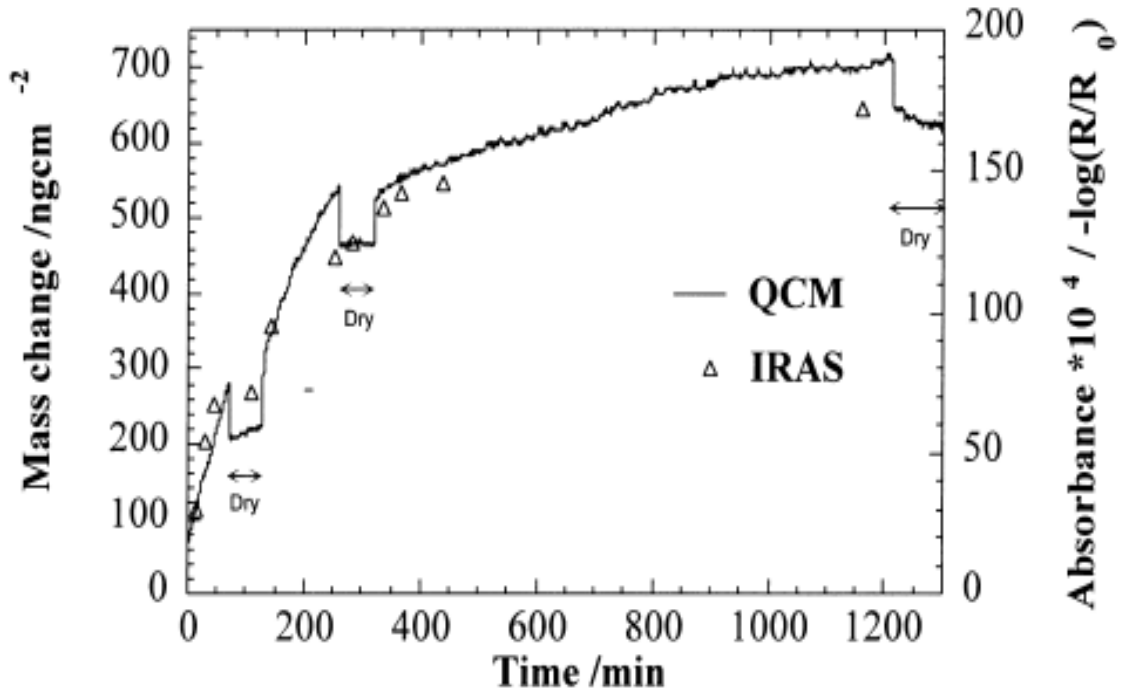

Figure 1.1 In Situ IRAS and QCM measurements of Cu_2O film formation reproduced from reference 3.

Persson et al. model their IRAS data for cuprous oxide film formation using a 4-layer model which utilized known frequency dependent optical indices of refraction for Cu_2O, bulk H_2O and metallic Cu.[4] In this model, the response of reflected IR is used to estimate oxide thicknesses between 10 and 15 Å with a physisorbed water layer 5 monolayers thick. The oxide film is chemisorbed to the Cu metal in this instance, and the

physisorbed aqueous adlayer sits atop the oxide film.[4] **Figure 1.2** gives a schematic illustration of this model. The techniques used, however, eventually start to probe into the bulk region of the sample. A more sensitive surface probe is needed to probe into the in situ kinetics of oxide formation.

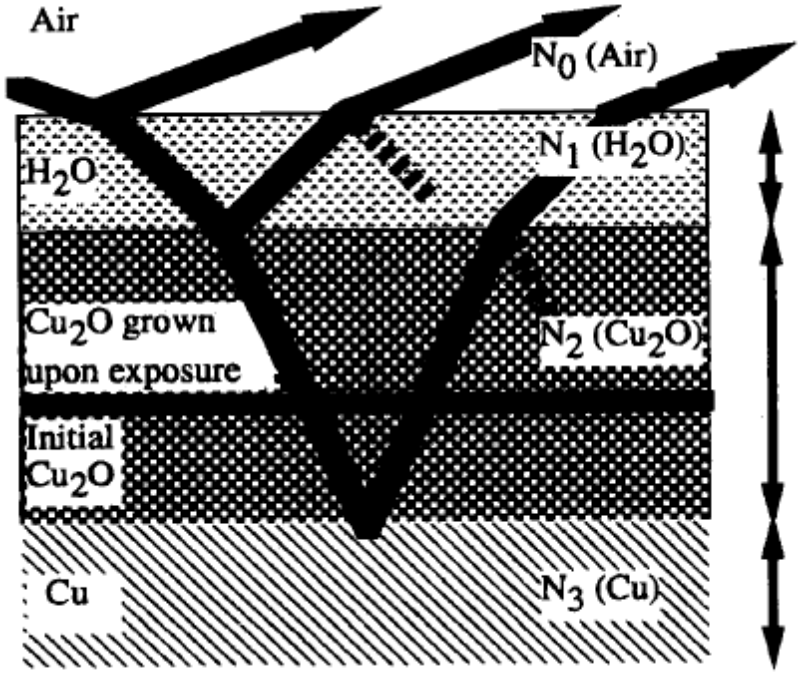

Figure 1.2 Four-layer model of cuprous oxide film formation reproduced from reference 5. The oxide coated surface may be modeled as the reduced metal coated with a thin chemisorbed oxide film with a physisorbed adlayer. The physisorbed adlayer is again shown to affect the rate of oxide formation.

To this end, second harmonic generation (SHG) is considered. The probe is a highly sensitive in situ probe which has been used to study various different surface properties of metallic,[6-11] dielectric,[8,12] liquid,[13-15] and colloidal[16-20] substrates to name a few of many examples. The technique has been used to probe metals under Ultra High Vacuum (UHV),[9,21] electrochemical,[22-24] and ambient conditions.[13-15,25-28] It has advantage of having submonolayer sensitivity along with relative experimental simplicity. In an electrochemical study done by Baten and coworkers in 2007,[24] in situ electrochemical SHG experiments were performed under basic conditions while sweeping the potential from -1.0 V to 1.0 V coinciding with Cu_2O and CuO formation. Upon initial Cu_2O formation, the authors note an increase in SHG signal may be due to a resonant enhancement at the Cu_2O band gap energy (2.1 eV).[24] An increase in oxide film thickness can lead to an increase in SHG due to signal emanating from the film itself. It is useful to also look at another example of adsorption kinetics presented by Zhu and Shen.[7] Increased exposure to a CO layer causes an observed exponential decrease in SHG signal due to decreased free electron density from the Cu(111) substrate. It is illustrative to present this example below in **Figure 1.3.**

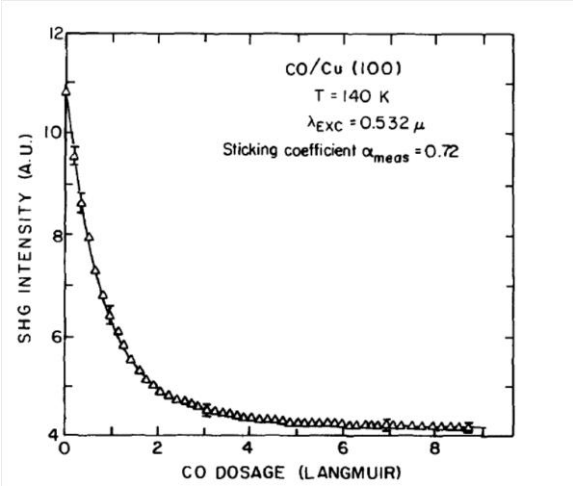

Figure 1.3 SHG as a function of CO exposure on Cu(111) at 140 K reproduced from reference 7.

Alkanethiol self-assembled monolayers (SAMS) are notable for their anti-corrosive properties and have been utilized as corrosion inhibitors.[29] Oxide formation has been probed using another nonlinear optical technique. Surface sensitive IR-Vis sum frequency generation (SFG) has been used to monitor oxide film formation for octadecanethiol (ODT) bound to polished Cu.[30] Over the course of 10 hours, the three peaks in the spectrum are observed to change in phase, and after 10 h. the phase change stops to shift.[30] This spectroscopy probes the chemisorbed ODT, and as an oxide film is observed to grow, interference occurs between the metal, the oxide, and the adsorbed ODT.

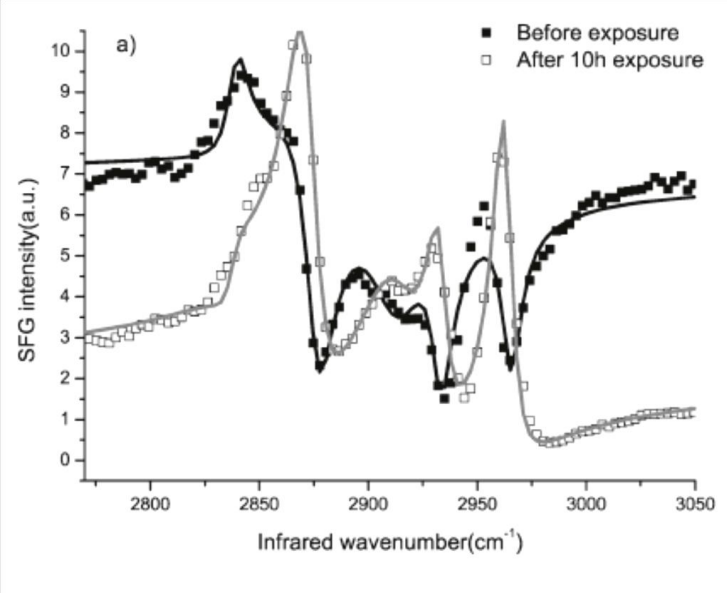

Figure 1.4 SFG spectrum of ODT adsorbed to Cu before exposure to dry air and after 10 h exposure to dry air. Reproduced from reference 30.

Second harmonic generation is a complimentary technique, and it has the advantage of only probing the metal substrate interactions along with the (electronically) resonantly enhanced oxide film. SHG is a surface sensitive nonlinear optical technique which for the purpose of the series of experiments presented in this thesis is used to probe the in situ electronic reorganization and analogously the adsorption kinetics of cuprous oxide film formation on Cu subjected to both dry and humid conditions as well as ODT bound to Cu under humid conditions. With that being noted, a basic theoretical description of SHG is warranted.

Chapter 2 provides a brief introduction to the surface sensitive technique of second harmonic generation. Examples are shown which demonstrate the submonolayer

sensitivity of the technique, and furthermore examples are provided which demonstrate SHG's ability as an in situ probe of adsorption kinetics on metallic substrates. Chapter 3 details the physical hardware and its characterization for the series of SHG experiments performed. The excitation source and its spectral and temporal characteristics are measured. Experiments are then carried out in reflection geometry on materials which possess bulk nonlinearity to ascertain the ability of the system to detect SHG. The experimental setup is described in detail. Experiments are then carried out on isotropic metallic substrates to determine the ability of the system to detect interfacial SHG. Since a slight modification is made in the experimental setup, a different experimental setup is described along with a brief description of the data acquisition software which is used to read the signal emanating from the detector.

Chapter 4 describes a series of experiments performed on a metallic Cu substrate. Oxide film growth is observed in situ using SHG on samples exposed to dry air and humidified air. Finally, oxide film growth is monitored with ODT adsorbed on Cu under humid conditions. ODT formation is checked with SFG, and oxide film growth is monitored with SHG.

Chapter 2: SHG Theory and SHG from Metallic Substrates

Second-order nonlinear optical techniques such as IR-Visible sum frequency generation (SFG) and second harmonic generation (SHG) have proven useful probes for the study of surface and interfacial phenomena. These techniques have allowed for the study of an extensive variety of interfaces including the gas-liquid, solid-liquid, gas-solid, and buried interfaces between two like phases.[14,21] The surface specificity of such techniques lies in the second-order nonlinear optical response from the interface itself.[31,32] A nonlinear optical response may be induced in a medium under influence from an electric field of about 1 kV/cm which may be readily obtained from a pulsed laser. [33,34] Under the electric dipole approximation, the nonlinear optical response of a medium may then be regarded as a Taylor Series expansion of the polarization (SI units), ε_0 is vacuum permittivity, $\chi^{(n)}$ is the nth order susceptibility and ω is the circular frequency of the field:

$$P(r, \omega) = \varepsilon_0 (\chi^{(1)} : E(r, \omega) + \chi^{(2)} : E(r, \omega) E(r, \omega) + \chi^{(3)} : E(r, \omega) E(r, \omega) E(\omega,t) + ...)$$

The lowest order nonlinear optical response $P^{(2)}$ is of particular interest for SFG and SHG.

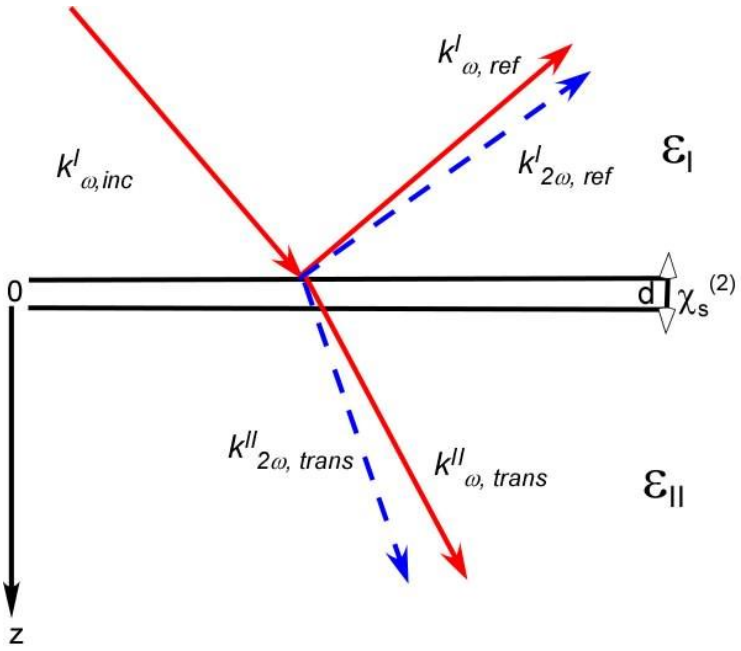

Figure 2.1 A plane wave travelling through medium I with wave vector $\mathbf{k}^{\mathbf{I}}_{\boldsymbol{\omega}}$ strikes the boundary between phase I and phase II characterized by ε_I and ε_{II} respectively. At this boundary, a sheet of nonlinear polarization $P^{(2)}_S = \chi_s^{(2)} : EE$ of vanishing thickness d is generated, and a second harmonic wave is generated in both reflected and transmitted directions.

At the interface between centrosymmetric media, an incident electromagnetic plane wave induces a sheet of nonlinear polarization which may be described as:

$$P_s^{(2)} = \varepsilon_0 \chi_s^{(2)} : E(\omega)\, E(\omega)$$

where $\chi_s^{(2)}$ is the second-order susceptibility tensor which entails the dipolar second-order response from the interface.

To discuss the surface sensitivity of second order nonlinear optical techniques, it is useful to consider the general case of the second order dipole polarization. $P^{(2)} = \varepsilon_0 \chi^{(2)}:EE$ Under inversion, this relationship becomes: $-P^{(2)} = \varepsilon_0 \chi^{(2)}:(-E)(-E)$

$-P^{(2)} = \varepsilon_0 \chi^{(2)}:(E)(E) \leftrightarrow -P^{(2)} = P^{(2)}$

Therefore $\chi^{(2)} = 0$ if the medium in question possesses a center of inversion. At an interface, inversion symmetry is broken. Thus, second order nonlinear optical techniques are surface sensitive under the electric dipole approximation.

The reader is referred to an excellent review by Heinz and numerous publications by Shen which solve Maxwell's equations for both the local (electric dipole) and nonlocal (electric quadrupole and magnetic dipole) SH fields generated by an induced nonlinear polarization.[8,32] Particularly in the reflected direction, the dipolar (surface) response is said to dominate.[35,36] SHG has been used to probe molecular adsorbates,[8] interfacial solvation dynamics,[37] and buried semiconductor interfaces[38] to name a few of many examples.

SHG has also been utilized in many instances to probe metallic surfaces. Tom et al. showed that the observed SHG response from metal surfaces under UHV conditions could be directly calibrated and compared to other more previously established surface science techniques like LEED and TPD.[6] For the particular case of Rh(111), they showed that O_2 adsorbed to the surface via a top site and that the adsorption corresponded to a simple Langmuir model.[6] The SHG signal was observed to decrease upon adsorption of O_2 and increase upon adsorption of alkali metals like Na.[6] In this instance, the SHG

signal is believed to arise from the oscillation of nearly free electrons at the surface of the metal. In the particular case of Rh(111), the surface electronic response was dominated by the metal substrate and chemisorption of adsorbed O_2 caused a depletion in the number of free surface electrons.[6] Analogously, when the adsorbate donates electrons to the substrate, the SHG signal will increase.

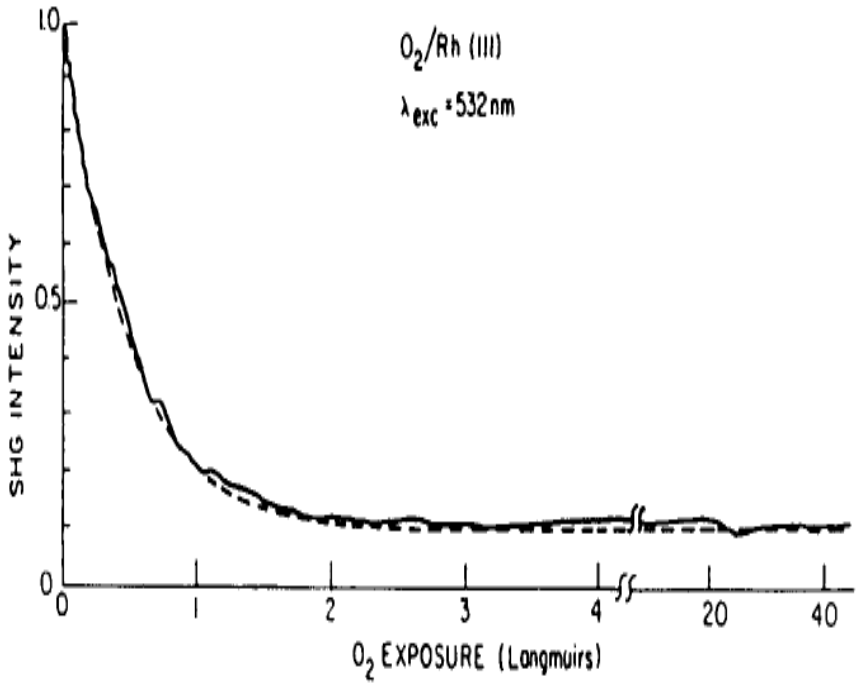

Figure 2.2 In situ monitoring of O_2 coverage on Rh(111) using SHG; reproduced from reference 6.

A free electron model may be used to model the SH response in which the electrons are assumed to be bound by slightly anharmonic potentials. The majority of the response from the metal surface again arises from free electrons, and this response may be altered

in the presence of molecular adsorbates. If the excitation or second harmonic wavelength is near an electronic resonance, the SH signal can also be enhanced, and the observed SH response can be assumed different.[22]

$$\ddot{x} + \omega_0^2 \dot{x} + \zeta x^2 = \frac{e}{m}[E(\omega)\cos(\omega t)]$$

Since the second-order nonlinear polarization is equivalent to the tensorial product of the second order susceptibility, the nonlinear susceptibility from this free electron model may be approximated as:[22]

$$\chi^{(2)} = -\zeta \frac{Ne^3}{2m^2} \frac{1}{(\omega_0^2 - 4\omega^2)^2(\omega_0^2 - \omega^2)^2}$$

ζ is the anharmonicity of the potential, ω_0 is the resonant frequency, ω is the driving field's frequency, N is the number of oscillators, and m is the mass of the oscillator. Again, as can be seen for this particular instance, the second harmonic signal from the metal substrate should be quadratically proportional to the number of free electrons at the surface. If the driving field's frequency is on the order of the surface Plasmon frequency, the signal will be resonantly enhanced according to this simple free electron model.

Chapter 3: SHG Instrument and Characterization

i. Laser System and Characterization

A Ti:Sapphire oscillator (Photonics Industries TFO 100) was used as the excitation source in the series of SHG experiments. This laser is optimum due to the high repetition rate and short pulse duration which can allow for higher peak powers to drive the second-order nonlinear response. Briefly, a 6.5 W frequency doubled cw 532 nm Nd:YVO_4 laser was used to pump the Ti:Sapphire oscillator. A schematic diagram of the system is shown in **Figure 3.1.** Vertically polarized light from the pump laser is steered into the oscillator cavity via a periscope which flips the input polarization of the pump beam to horizontal. This light then passes through a Brewster window BW1 and is steered and focused by PM1, PM2, PM3, and L1 through a folding mirror M1 onto a Brewster cut Ti:Sapphire rod which, when properly aligned, will emit and reflect of M1 and M2. The near IR beam will then be simultaneously directed to M2 and a Brewster cut prism pair used to introduce negative group velocity dispersion into the laser pulse. After the prism pair, the beam is sent to a variable aperture slit and reflected off of mirror M3. The beam will then emerge from the laser cavity at the output coupler OC which then directs the beam to BW2 which insures that the output polarization of the laser is horizontal with respect to the plane of the optical table.

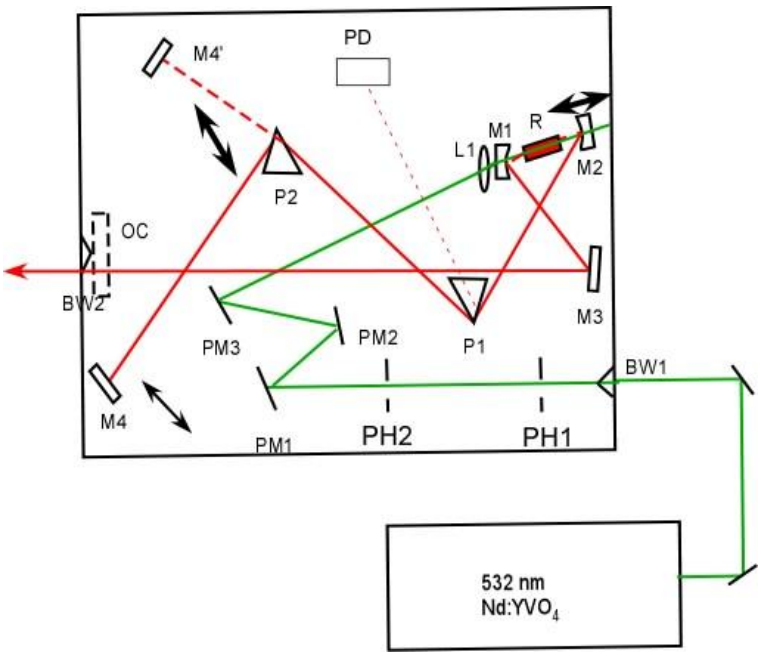

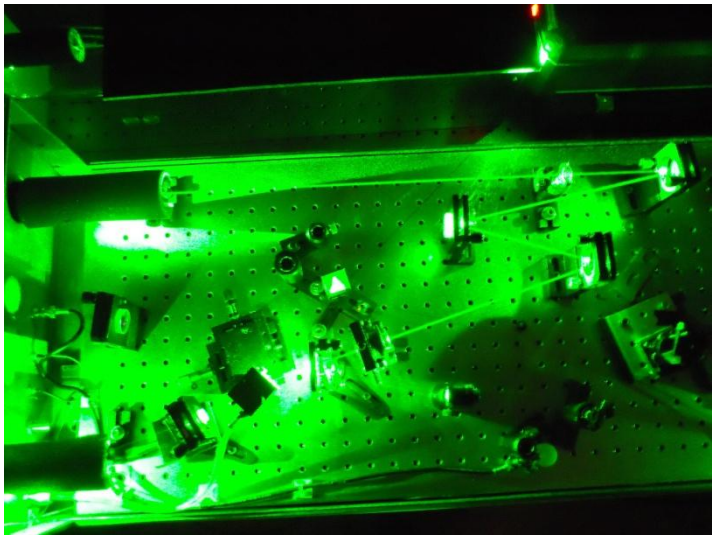

Figure 3.1 Optical layout and photograph of Photonics Industries TFO-100 pumped by Coherent Verdi V6, BW – Brewster Window, M – near IR mirror, PD – photodiode, PM – pump mirror, PH – pinhole, P – negative group velocity prism, OC – output coupler, PE1 and PE1 are steering mirrors before BW1.

The output pulse train is monitored by a fast Si photodiode which is read by a 350 MHz Tektronix oscilloscope. From this, the repetition rate of the laser has been measured at 78 MHz. To further characterize the laser pulse, the output pulse was attenuated and dispersed by a Hg lamp calibrated spectrograph onto a 1024 pixel CCD array. Calibration details for the CCD array are presented in **Figure 3.2.** From the calibrated CCD array, the center wavelength of the output pulse was estimated to be 798 nm with a 7.36 nm spectral bandwidth. General operating procedures for the TFO-100 are provided.

1. Turn on the chiller for the Coherent Verdi V6 laser, and allow this to cool to 20 ^{o}C before turning the key to on from standby; the laser power should be set at 0.01 W.
2. If the laser has not been installed, align the beam using the periscope mirrors PE1 and PE2 using PH1 and PH2 respectively. Use a floating pinhole to check the beam alignment throughout the laser.
3. Remove the lens L1, and steer the green beam into the center of the rod, and adjust the position of the beam through the rod until maximum transmission and minimum reflection is observed; the beam should pass through the center of the laser rod along the crystallographic axis. Check the backreflection of mirror M1 using the floating pinhole.
4. Replace the lens L1, and adjust the backreflection of the beam off the lens using the lens holder; the position of the beam should remain the same throughout the

rod. Adjustments can be made by moving the rod to insure minimum reflection. Check the height of the green beam using the floating pinhole by placing the beam both behind prism P1 and in front of prism P2. Adjust the position of the beam behind prism P1 using Mirror M2, and adjust the position of the green beam before prism P2 by adjusting the P1 stage.

5. After the green beam is aligned, turn the laser power up to 5 W. Move prism P2 out of the way, and use a Near IR viewer to check the fluorescence of the beam. Adjust the back reflection from mirror M4' and OC. The back reflection from mirror M4' should be slightly off. Continue adjusting until lasing is achieved.
6. Move prism P2 into the beam path, open the slits in front of mirror M4, and adjust the backreflection off of this mirror until lasing is again achieved. Optimize the cw power, and check to make sure that a small backreflection off prism P1 is aligned into the Si fast photodiode. Connect the photodiode to an oscilloscope of at least 300 MHz bandwidth.
7. After cw power has been optimized, close the slits in front of M4, and adjust the micrometer position of mirror M2 in the direction away from you by a small amount. To achieve modelocking, hit the prism. If modelocked, a pulse train will appear on the oscilloscope. Adjust the OC and Mirror M4 to achieve an optimum pulse train.
8. If the beam has not been characterized, the spectrum can be checked by dispersing the pulse via a grating onto a calibrated CCD array. The pulse duration can be checked via autocorrelation.

The electronic response time of the photodiode is too slow to be able to resolve the pulse duration, but it does provide an indication that the laser is modelocked. From the oscilloscope/ fast photodiode combination, it is determined that the repetition rate of the oscillator is 78 MHz. The intensity of the laser pulse is determined by a laser power meter (Molectron), and at 5 W pump power, 300 mW average power has been measured. Dividing the average power by the repetition rate, this corresponds to an energy of 3.8 nJ. If the pulse duration is in the 100s of fs and the beam is focused down to 0.5 mm, peak power densities on the order of $\frac{MW}{cm^2}$ may be obtained.

Next, the pulse can be spectrally characterized by dispersing the pulse through use of a spectrograph (150 grooves/mm) onto a Princeton Instruments 1024 Pixel CCD cooled to -9°C. This device was calibrated using the 1st and 2nd order diffraction from the strong 405, 436, 492, 546, and 577 nm spectral lines of a Hg lamp. The calibrated spectrograph is used to determine the center wavelength. A plot of the calibration is shown in **Figure 3.2**. A pulse spectrum for a 798 nm pulse from the TFO-100 is shown directly underneath in **Figure 3.3.**

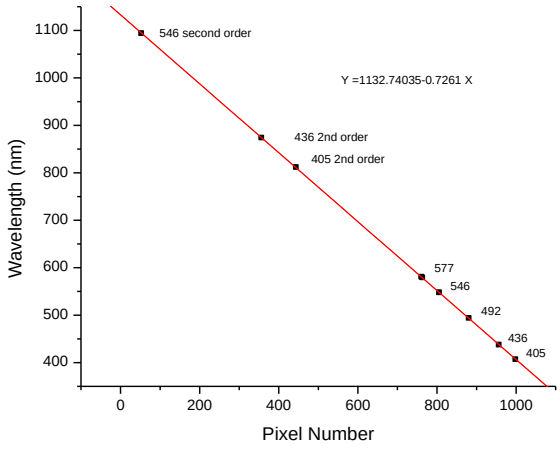

Figure 3.2 Hg lamp calibration of the spectrograph

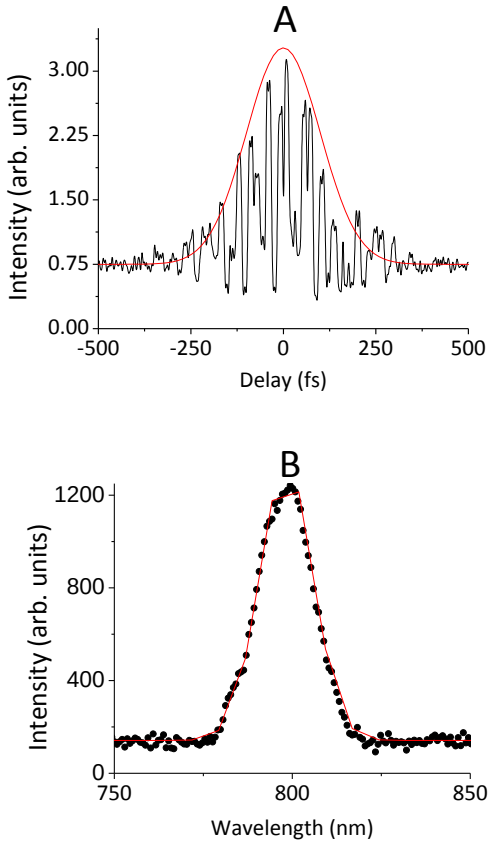

Figure 3.3 A: Autocorrelation trace of pulse train from the TFO-100 B: Spectrum

Spectral characterization of the laser pulse is not sufficient to provide an accurate estimation of the pulse duration, and the photodetectors available only have response times on the order of ns. In order to measure a short event, a material with a response time much shorter than that event must be utilized, or the signal can be measured against a much shorter even i.e. cross-correlated. When neither of these is available, the signal must be measured against itself. For this reason, an optical autocorrelator was built which employed a Michelson interferometer and a frequency doubling z-cut quartz crystal.

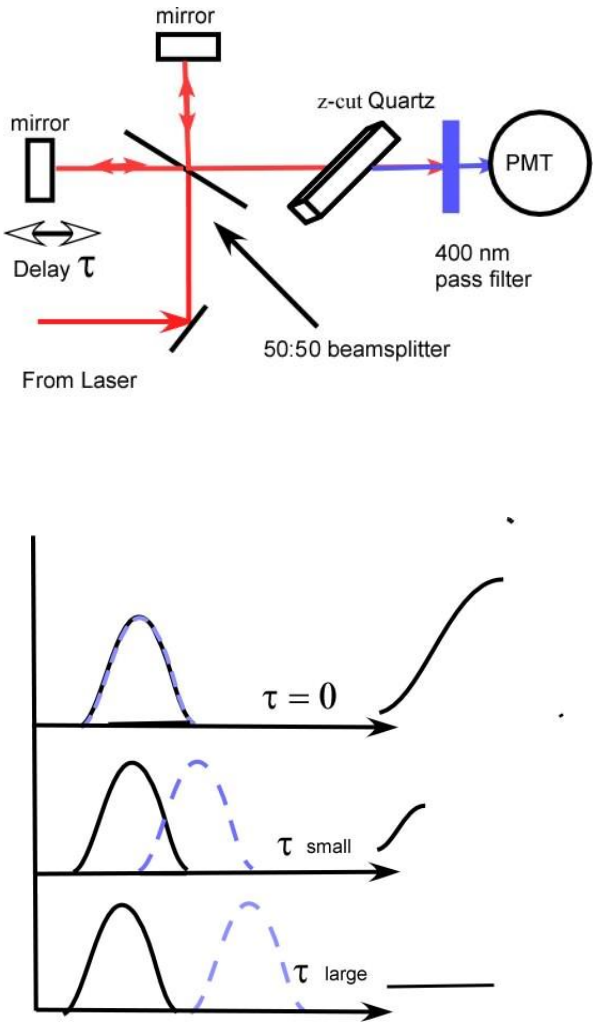

Figure 3.4 Top: Schematic diagram and of the Autocorrelator employed to estimate the pulse duration of the TFO-100. Bottom: Scanning the delay. When the pulses do not overlap, there is no autocorrelation signal. At zero delay, the autocorrelation displays maximum intensity.

An incident train of EM pulses from the oscillator are split in two by a 50:50 broadband coated beam splitter (Spectra-Physics), and the split pulse train is reflected off two equivalent mirrors. The delay is scanned by stepping the movable mirror on an

optical rail (Velmex Unislide), and the recombined pulse train is then upconverted to the SH via a 1mm thick z cut-SiO_2 crystal. The remaining fundamental is filtered off via a 400 nm narrowband pass filter, and the SH is subsequently detected by a PMT (Hamamatsu R212) and sent to a picoammeter which is connected to a DAQ device for signal acquisition. If the delay is scanned slowly enough, the time averaged signal measured by the detector is the second-order interferometric autocorrelation function, and this is given by:

$G_2(\tau) = \int_{-\infty}^{\infty} \langle | [E_1(t-\tau)+E_2(t)]^2 |^2 \rangle \, dt$ where E_1 and E_2 are the electric fields of the two split pulses, and τ represents the temporal delay and $\langle . . \rangle$ indicates an average. Fringes arise from interference of the two overlapped SH pulses emanating from the crystal at $2d = m\lambda$ where m is an integer multiple of the SH wavelength. Again, the detector measures, the averaged intensity. The FWHM of the observed autocorrelation trace is measured, and this is multiplied by a deconvolution factor of 0.65 for an assumed $\mathrm{sech}^2(\tau)$ pulse shape. The stepping motor which controls the delay stage was calibrated at 2.40 ± 0.5 μm / step = C, and the autocorrelation delay may be calculated by first calculating the distance traveled by the delay stage and then by using this delay as the coherence length of the laser pulse which in turn can give the temporal delay. To calculate the coherence length $d = C\ T\ N$ where N is the stepper motor speed, and T is the amount of time the delay stage has travelled. The temporal delay or coherence time may then be calculated by using this coherence length $\tau = 2\ d\ c^{-1}$; c is the speed of light in vacuum.

Figure 3.3 provides the spectrum of the pulse and an interferometric autocorrelation trace of the pulse train. As has been noted, the pulse corresponds to a central wavelength of 807 nm, and the pulse duration is found to be 153 fs by first measuring the FWHM of the envelope of the trace to be 235 fs and then multiplying by a 0.65 deconvolution factor for the assumed $sech^2$ pulse shape. The pulse shapes are assumed because phase information cannot be extracted solely based on autocorrelation.[39] All of the fringes are not resolved on the interferometric autocorrelations because the minimum step size is too large, and the motor does not step linearly at very low speeds. The interferometric autocorrelation trace was acquired by stepping the motor 1 step $(2s)^{-1}$.

ii. SHG Characterization

Before performing any surface specific experiments, a series of experiments were run to test both the quadratic intensity dependence of the SHG signal and to reproduce the anisotropic rotational response from the GaAs (100) face. The setup used in those experiments is presented here.

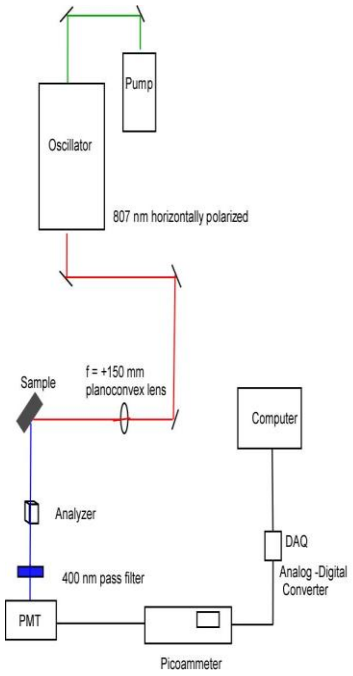

Figure 3.5 Optical layout of SHG experiments in reflection from noncentrosymmetric substrates

The incident radiation from the Ti:Sapphire is gently focused onto the sample surface at an incident angle of 45° using a f = +150 mm plan convex lens. From there the laser light is passed through a Glan-laser polarizer, and it is subsequently filtered by a

400 nm $\pm$ 15 nm pass filter (Omega Optical), En route to the PMT, another 400 nm filter is utilized, and the photocurrent from the PMT is read by a picoammeter whose voltage output is interfaced to a computer via an analog to digital converter DAQ device (Futek DAQ 300). Initial tests of the detection electronics for detection of an SH signal were performed on two materials which possess bulk nonlinearity. The detection system is the same as employed in the autocorrelation measurements. The photocurrent generated by SH photons reflected off of α-Quartz demonstrate quadratic dependence on the incident intensity, since $I_{2\omega} \propto |\chi^{(2)}E_{\omega}^{2}|^{2}$ i.e. $I_{2\omega} \propto I_{\omega}^{2}$. This intensity dependence was measured in the reflected direction and is presented in **Figure 3.6**.

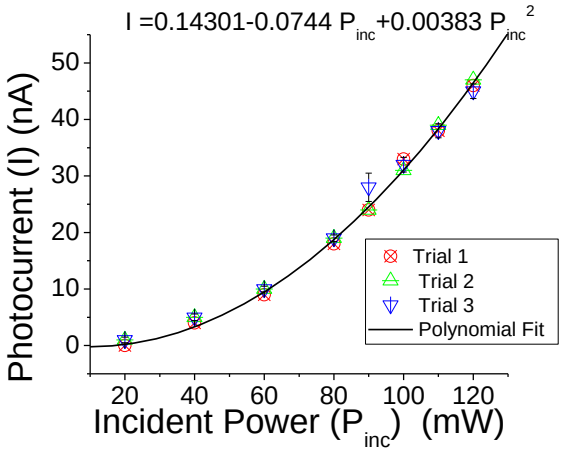

Figure 3.6 Intensity dependence of reflected SH on intensity of the fundamental at 45 degree angle of incidence on z cut–SiO_2. The observed intensity dependence is quadratic indicating that the photocurrent response of the PMT is indeed generated from the SH.

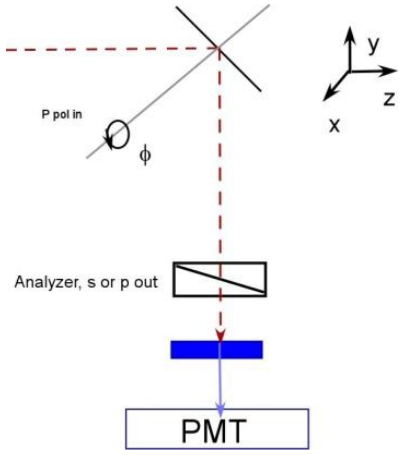

Figure 3.7 Sample orientation and experimental geometry for SHG from GaAs

GaAs (100) was rotated about the surface normal as indicated above; the angle of incidence was 45.^{o} This was done to access different crystalline orientations hence, different elements of $\chi_{ijk}^{(2)}$. GaAs is noncentrosymmetric, and as a result the SH signal originating from the bulk should be large. Since GaAs is a cubic structure of zincblende type, the bulk susceptibility tensor only has one term.[40] The index i corresponds to the SH field's polarization, and j and k are degenerate due to the permutation symmetry of the two input fields. An analyzer was employed to discriminate the SH response from these different elements of the second-order susceptibility tensor. P in: s out, and p in: p out polarization combinations were measured. According to Shen et al.,[41] the surface structure of the noncentrosymmetric substrate can be probed by using polarization analysis. For the p in: pout combination the different elements of the surface tensor which are analyzed are zzz in the 100 direction and zzz and yxx for the 110 direction. For the p in: s out combination, the tensor elements analyzed are yyz = xxz for the 100 face,

xxz = xzx, yyz = yzy, xxy = xyx, and yzz for the 110 face of the crystal.[41] The observed SH intensity pattern for the p in: s out polarization combination reproduces the work of Armstrong and Yamada. [40,42] For the SH intensity pattern from the p in: s out combination, a phase shift was observed from the p in p out combination. The observed difference in peak intensity as a function of angle is due to the fact that different angles of incidence were employed in the experiments. The SHG intensity pattern can be fit to a sinusoidal function based on Bloembergen's model.[43]

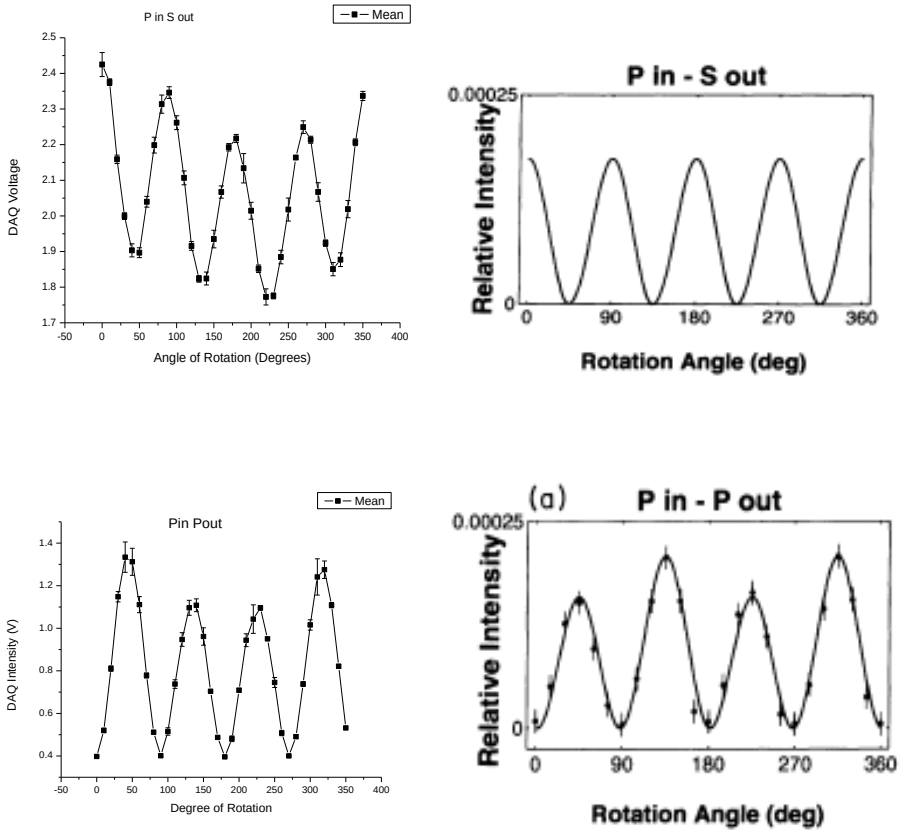

Figure 3.8 Left: SH from GaAs(100) as a function of rotation about the normal to the plane of incidence. Right: GaAs (100) rotational plots reproduced from reference 40.

The above experiments showed that the laboratory has a system capable of measuring SHG. Since the above materials were noncentrosymmetric, the second-order nonlinear response is allowed in the bulk. A general scheme for detecting SHG in reflection is presented below in **Figure 3.9.** This setup without a polarizer was used for both the quadratic dependence experiments and the polarization dependence of the signal from gold.

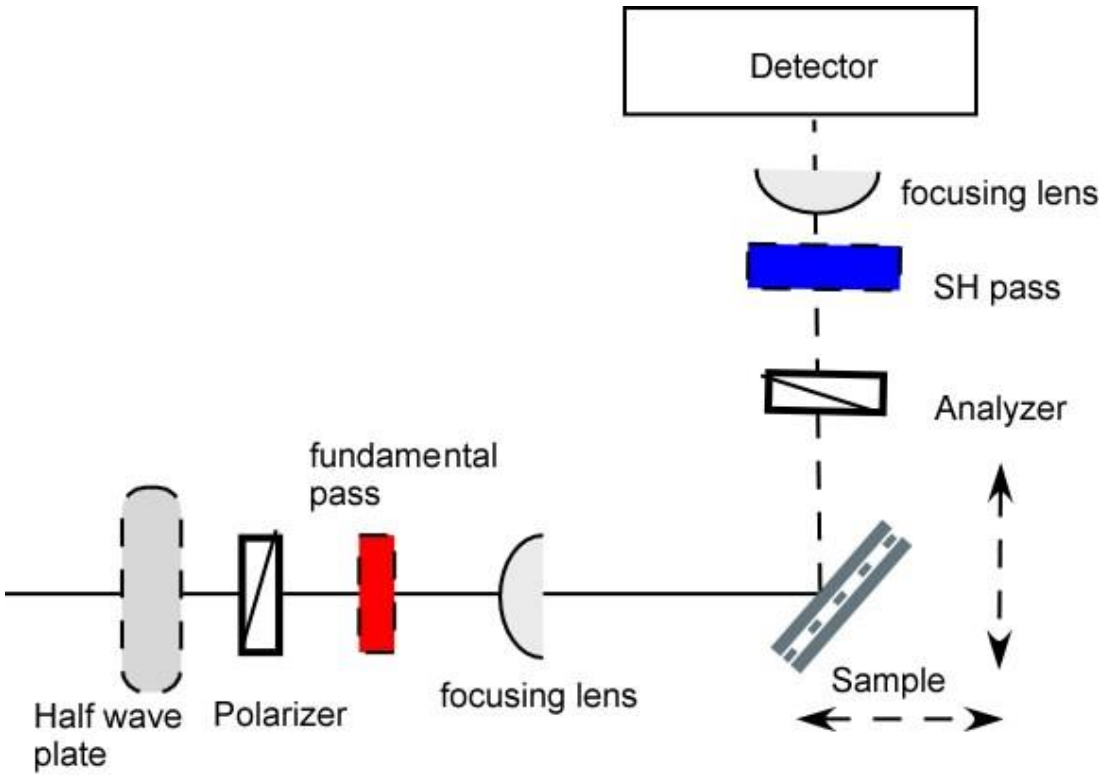

Figure 3.9 General reflected SHG experiment

To ascertain the validity of the system for surface studies, initial quadratic and polarization dependence of the SH signal from an evaporated film of gold was obtained. **Figure 3.10** shows the quadratic dependence of the SH signal on incident laser power

from an evaporated gold film. Based on this quadratic dependence, the signal at the detector can confidently be assigned as SHG. This step shows that the instrument is sensitive enough to detect SHG from a surface.

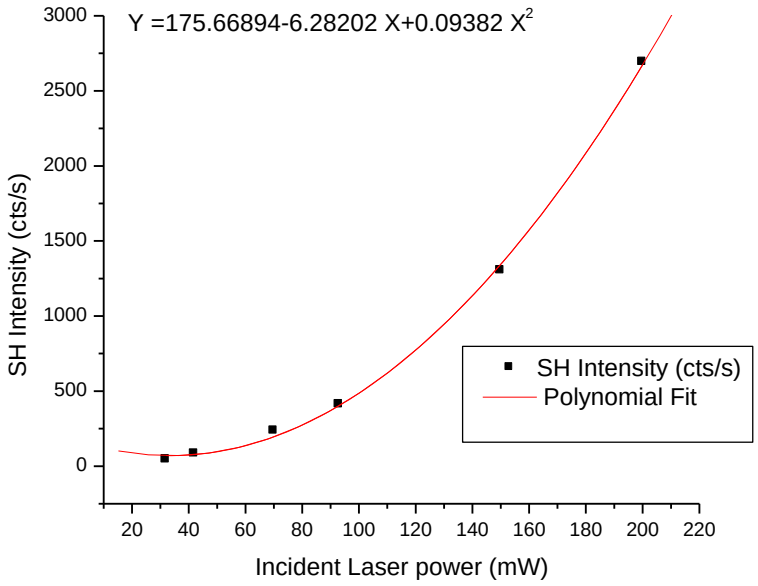

Figure 3.10 Quadratic dependence of intensity on incident laser power.

As a last step in surface SH characterization, the polarization response from an evaporated gold film was measured. As seen in **Figure 3.11,** the polarization combination of p in: p out gives maximum signal. For p in: p out polarization, laser light passed through a half waveplate, and the signal detected was passed through an analyzer set to pass horizontal polarization to the detector. For p in: s out polarization, the analyzer was rotated by 90° to allow vertical polarization to pass to the detector. For s in: p out polarization, the half waveplate was rotated by 45° to change the input polarization of the

incident light beam; the analyzer was rotated to allow horizontal polarization to the detector. Finally, for s in: s out polarization, the half waveplate is set to rotate the plane of polarization of the incident beam, and the analyzer is set to p as vertically polarized light to the detector. As seen in **Figure 3.11,** the polarization combination of p in: p out gives maximum signal.

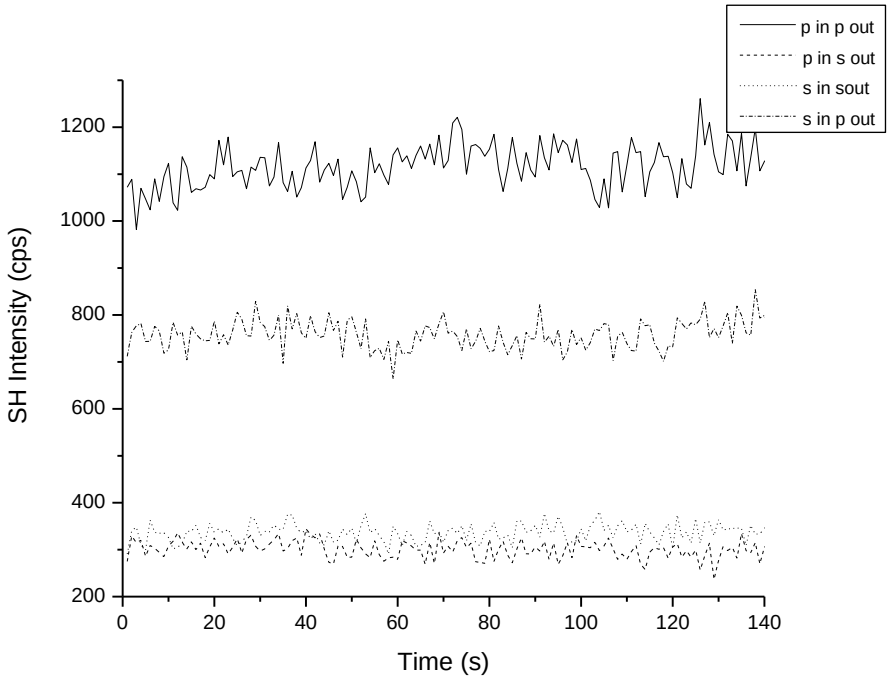

Figure 3.11 Polarization dependence of SHG from Au

iii. Final Experimental SHG Setup

For the SHG studies of copper, the waveplate and polarizer are removed to increase the signal to noise ratio. Horizontally polarized light from the Ti:Sapphire oscillator is split off by a thick glass plate, and this split beam is used to generate SHG

inside a 2.5 mm thick lithium triborate (LBO) crystal. This signal is monitored by a PMT (Hamamatsu R285) connected to a picoammeter which outputs a voltage to a USB interfaced analog to digital converter (Futek DAQ 300). This signal is monitored to account for any fluctuations in laser power. The other portion of the beam is steered to the sample and passes through an 800 nm bandpass filter to remove any spurious SHG before being gently focused by a 150 mm convex lens. The sample is mounted at 45 ^{o} with respect to the p-polarized incident beam inside a vacuum cell which has a CaF_2 entrance window and a fused quartz exit window. A schematic and photograph of the sample cell is shown in **Figure 3.15.** Subsequently, the beam of mixed output polarization is then passed through a 400 nm bandpass filter and sent to a monochromator attached to a photon counting PMT (Hamamatsu H6240-01). The TTL pulse train is then sent to a bnc connector (NI BNC 2121) which is connected to a PCI interfaced counter/timer board (NI 6602) where a Labview program counts the number of pulses sent by the PMT. Integration times using the Labview program can be set from 1/100th of a second. Typical integration times used in the following experiments are 10 s. The dark count of the PMT increases logarithmically throughout the experiment, so the laser signal must be periodically blocked to determine the dark count. After fitting a function for the temporal dependence of the dark count intensity, this signal is subtracted from the collected data. An illustration of the Labview vi used to collect the data is presented here. The front panel and block diagram are both displayed. In order to take a measurement, the integration time and total measurement time need to be entered into the front panel of the program. The program works by utilizing two counters and the internal frequency

base of the National Instruments counter timer board. Count rates up to 125 MHz may be used with this instrument. Measurements are ungated. An ideal way to gate the measurement would be to connect an optical chopper to trigger one of the gate channels on the bnc interface to the counter. Illustrations which demonstrate the computer interface of the data acquisition software is provided in **Figure 3.12**. A flow diagram which represents the total data acquisition route from the PMT to the Lab View data acquisition software is represented in **Figure 3.13**. As performed, the experiments required periodic manual blockage of the laser beam's path in order to properly be able to account for any noise emanating from the amplified PMT.

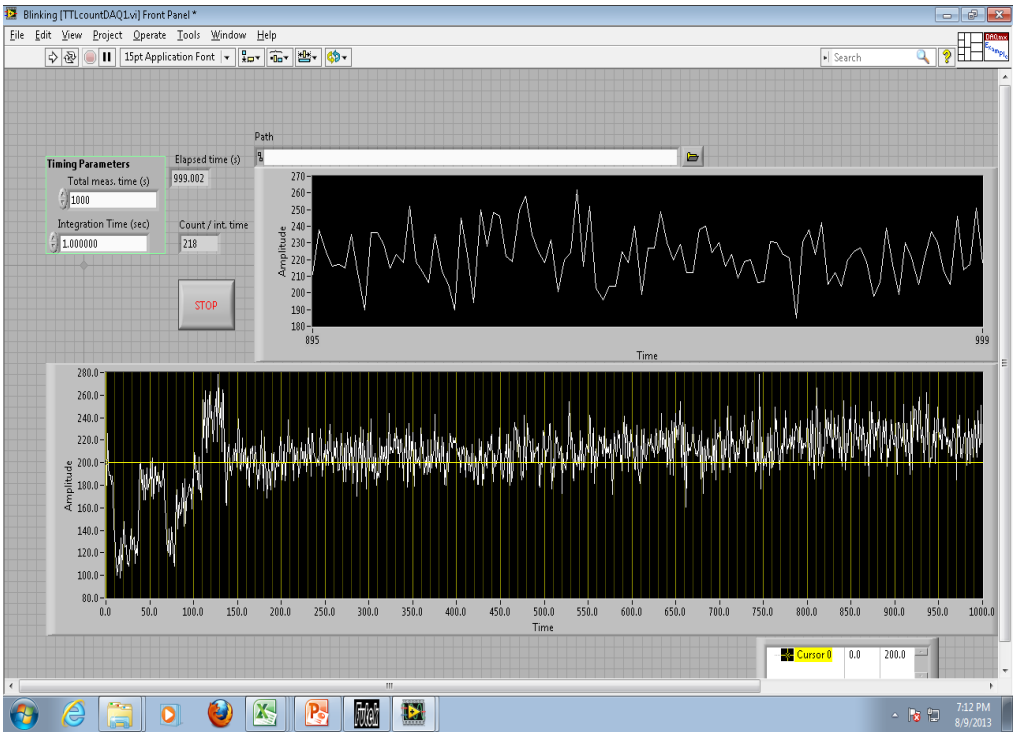

Figure 3.12 a Front panel of the Labview program used to count TTL pulses

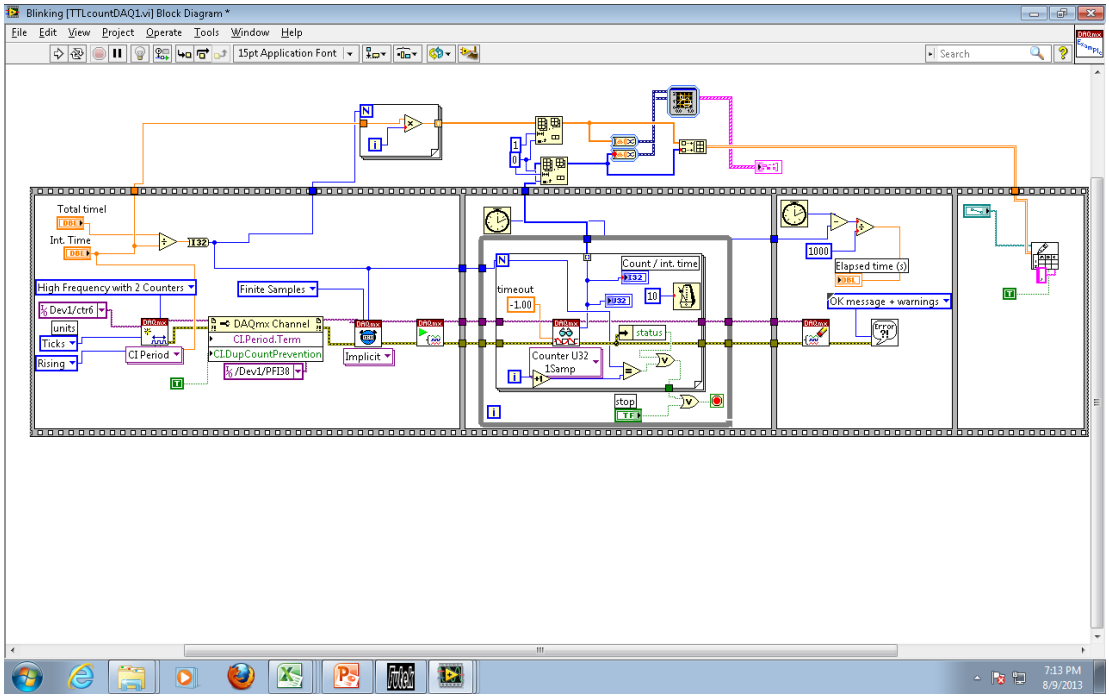

Figure 3.12 b Block diagram of the TTL edge counting program used to collect SH signal

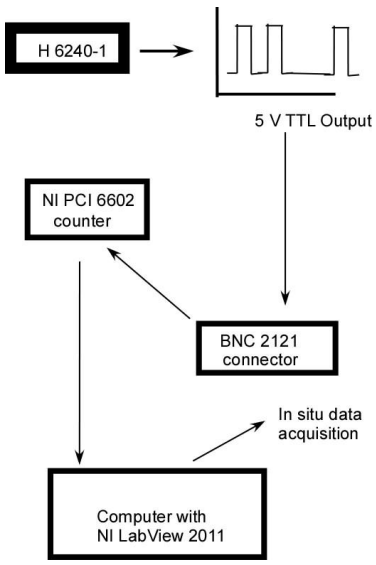

Figure 3.13 Flow diagram of data acquisition scheme from PMT to computer

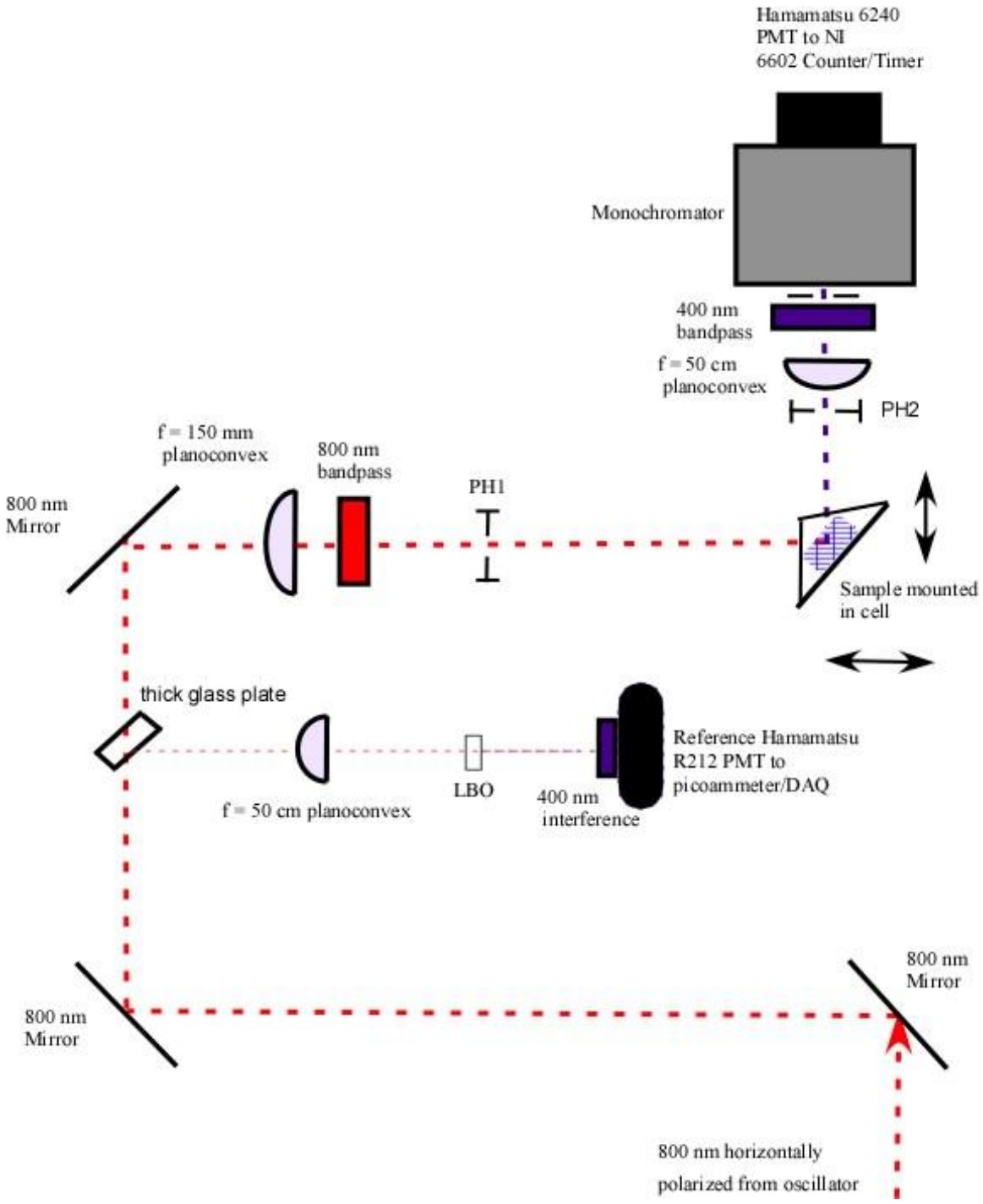

Figure 3.14 Optical layout of Reflection SHG experiment. PH1 and PH2 are pinholes used for alignment purposes.

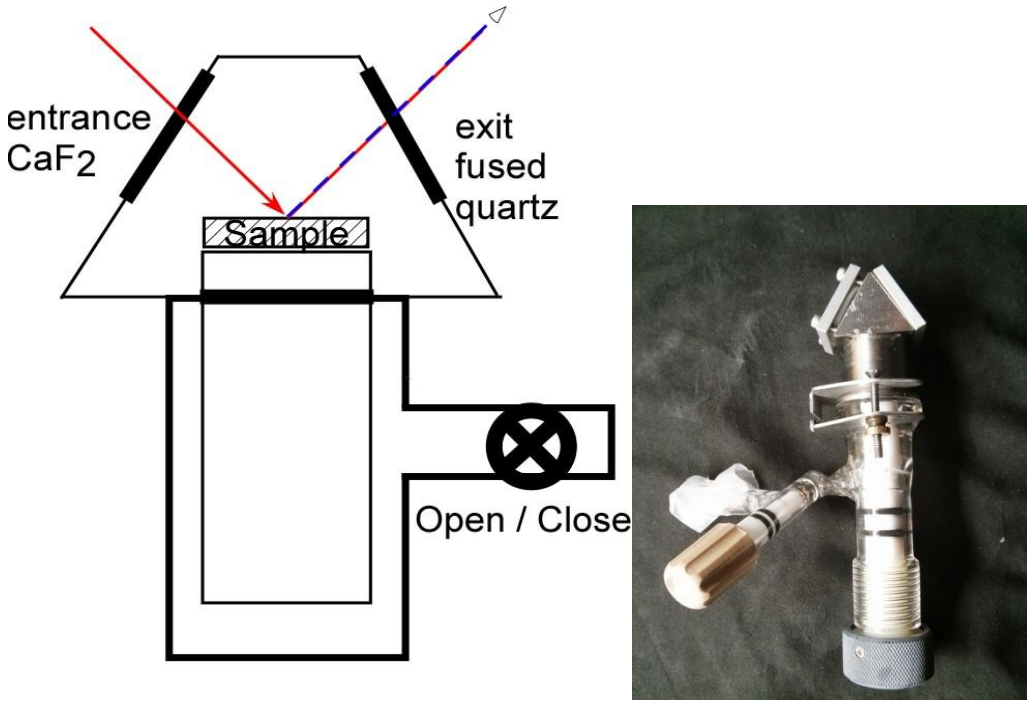

Fig 3.15 Schematic and photo of the sample cell used for the SHG experiments

iv. Data Processing

The noise count from the H6240-01 is not constant in time, so the laser beam is periodically blocked throughout the measurement to account for any additional noise in the measurement. As stated before, ideally, the high repetition rate laser source would be chopped, and the chopper would modulate a gate function over which the background signal could be programmatically subtracted. In order to account for the noise count, the dark count data is plotted using Origin software, and a function of the form:

$$I = I_0 + A_1\left(1 - e^{-t/\tau_1}\right) + A_2\left(1 - e^{-t/\tau_2}\right)$$

The fitted background function is then subtracted from the raw data to account for any noise in the measurement. An example fit to background noise is provided in **Figure 3.16.**

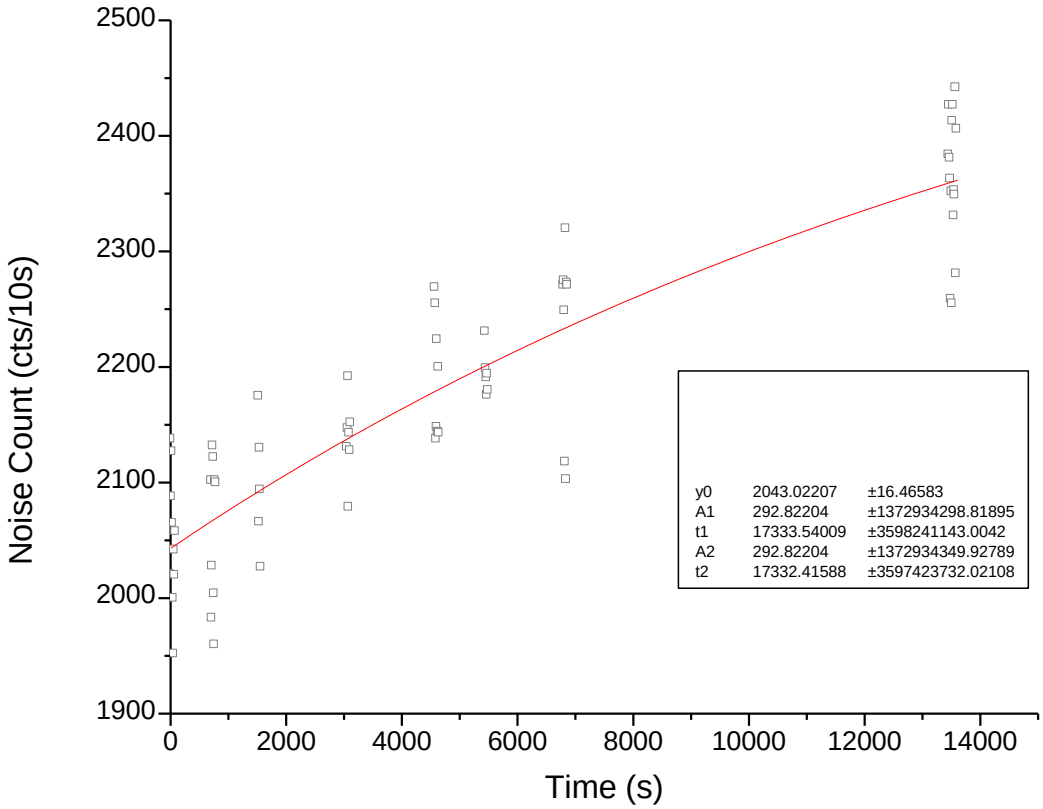

Figure 3.16 The noise was fitted to an exponential association function for later background subtraction.

A final step in data processing involves normalizing the signal to both the reference channel by dividing the background subtracted data by the signal observed by

the reference channel to account for noise. Finally, the signal at each data point is divided by the average signal before exposure. This is outlined in the following equation.

$$I_{SH}^{normalized} = \frac{(I_{SH}^{Raw} - I_{noise})}{I_{ref} I_{t<0}}$$

v. **SFG spectra**

SFG spectra were obtained on a previously described experimental setup.[44,45] Briefly, a 1064 nm Nd:YAG laser (EKSPLA PL2251 A) with a 19 ps pulse duration at 25 Hz repetition rate is used to pump a Laservision optical parametric generation/ optical parametric amplification system (OPG/ OPA) which is used to generate a 532 nm beam and tunable IR tunable from 2000 cm^{-1} to 4000 cm^{-1} using KTP crystal. These visible and IR beams are spatially and temporally overlapped at the sample in a copropagating direction at respective incident angles of 50° and 60°. The SF signal passed through an interference filter before and monochromator before being detected by a PMT and box car averaged. Spectra are obtained in the C-H stretching region from 2750 to 3050 cm^{-1} using a ppp polarization combination. The average of 3 scans is obtained to verify the presence of ODT on the Cu surface.

Chapter 4: Cu_2O Film Formation Monitored In Situ by SHG

i. Experimental

In order to prepare Cu samples for the SHG experiment, samples were cut into 20 mm x 20 mm squares and abraded by SiC paper to 2000. Samples were then polished with 6, 3, 1, 0.25, and 0.1 μm diamond paste and sonicated in ethanol after each step to remove the polish. Samples were then transferred to a N_2 purge box and dipped in amidosulfonic acid (ASA) to remove the native oxide film. Afterward the samples were rinsed in purged ethanol before being dried under N_2 and being mounted in the sample cell. For experiments with dry air, a bare copper signal was typically collected for 1000 s before a valve was opened to a bellow connected to coiled copper tubing immersed in a dry ice bath to condense any water which may be in the air. An isopropyl alcohol dry ice bath has a temperature of -77 °C, and at this temperature, the vapor pressure of water is 2.0×10^{-3} torr. Water vapor flowing into the coiled tubing will completely condense in this case. Samples were transferred from the glove box and evacuated to 9.0×10^{-5} torr. Exposure time zero is when the valve into the sample cell is opened to expose the sample to air in the environment.

ii. Results

For the first experiment, the sample was exposed to dry air, and the data acquisition programs were run for 12000 s. Data were collected for 1000 s before

opening the valve on the sample cell to allow in dry air. Raw and processed data for this measurement are shown below in **Figure 4.1.**

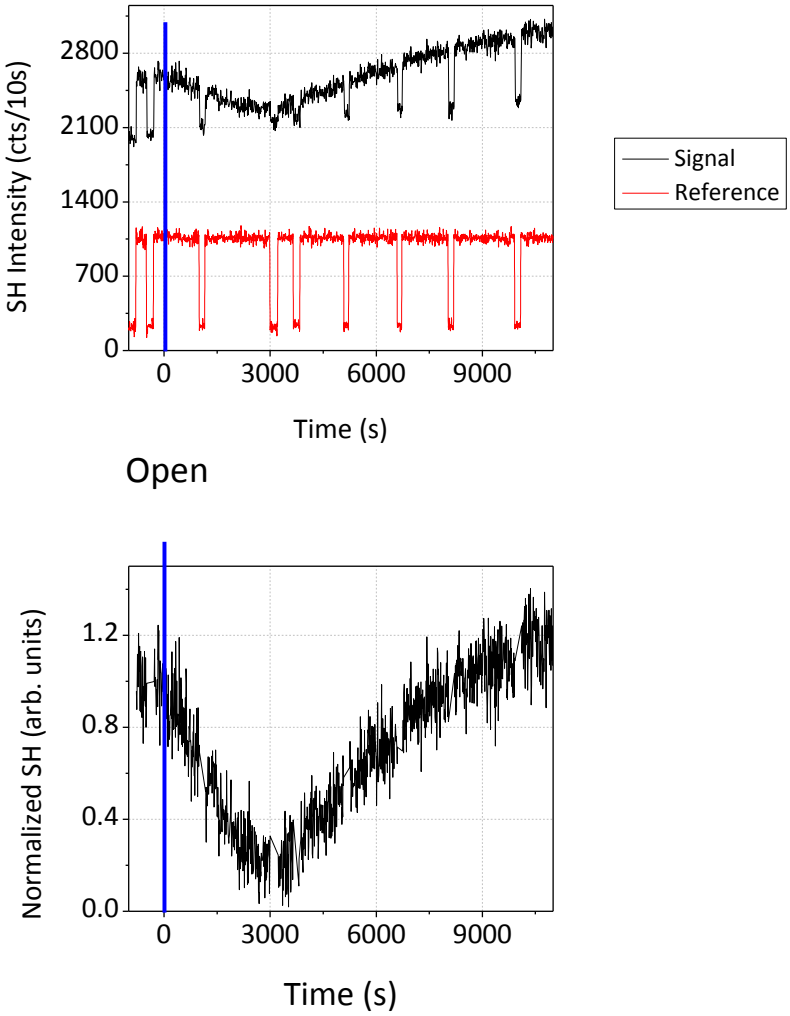

Figure 4.1 Top: Cu exposed to dry air with reference channel and noise count displayed. Bottom: Background subtracted SHG of Cu exposed to dry air vs. exposure time (s).

Initially the signal is seen to decay for 3000 s before the signal is observed to increase after the minimum in intensity is reached. The signal is postulated to plateau

10000 s after exposure, but further data points beyond the range obtained in this experiment are needed to verify this conclusion. The processed data are normalized to both the reference channel and the initial signal before exposure as detailed in Chapter 3.

A second trial of this experiment was performed for 22000 s, and the signal is observed to decrease for 3000 s after exposure and then increase and subsequently plateau. The final processed data plot normalized to the reference channel and initial signal for this trial is shown in **Figure 4.2**.

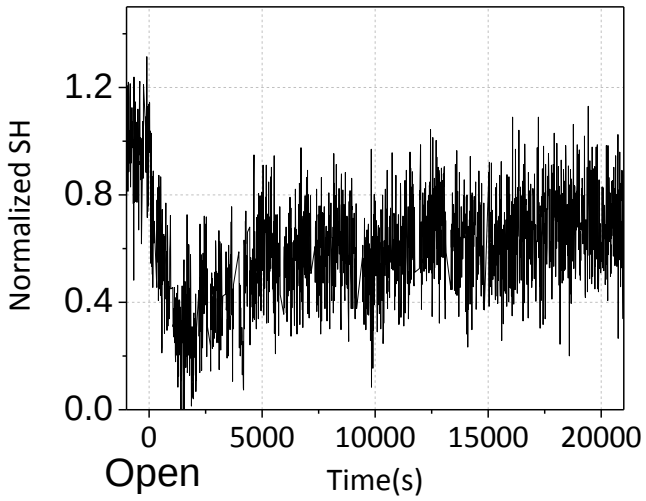

Figure 4.2 Cu exposed to dry air with 19000 s exposure time(s).

For humid air experiments, the same stripping procedure was followed with ASA, but in place of dry air, the valve was opened to air at 34 % relative humidity. The data acquisition program was set to run for 16000 s at 10 sec integration times between data points. Data from this run may be found in **Figure 4.3.**

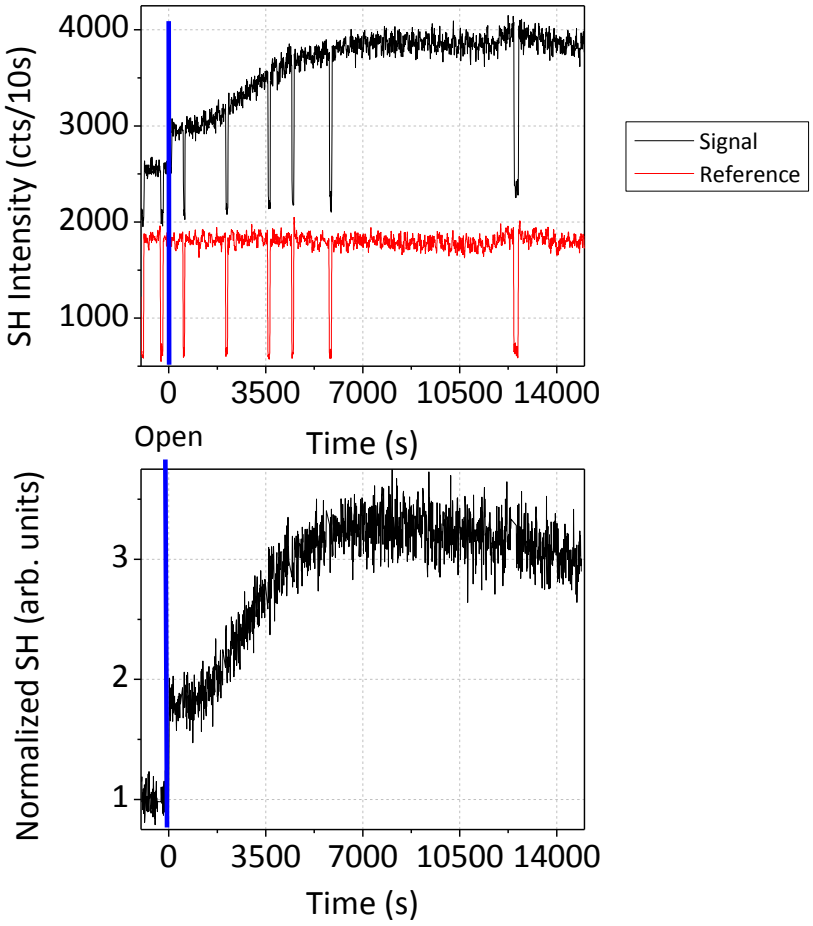

Figure 4.3 Top: SHG of bare Cu exposed to humid air raw data with reference channel; Bottom: Background subtracted data for SHG of bare Cu exposed to humid air.

Upon exposure to air, the signal is observed to jump to about 1.8 times the bare metal value immediately. The signal continues to rise until it peaks around 5000 s and begins to decrease slightly. Through the reference channel, it is seen that laser drift is present. The signal is normalized with respect to the reference channel to account for this drift.

ODT was purged with N_2 gas for 30 minutes before the ASA treated Cu was immersed in a 5 mM solution for 22 h and subsequently dried before mounting into the sample cell. Before running SHG, an SFG spectrum in the C-H stretch region was run to check whether the metallic substrate was reduced. This spectrum was checked versus reference.[30] Subsequent SFG spectra are shown along with the spectrum for partially oxidized Cu. Spectrum A&B correspond to a reduced Cu sample with ODT undergoing oxidation, and spectrum C corresponds to a partially oxidized substrate.

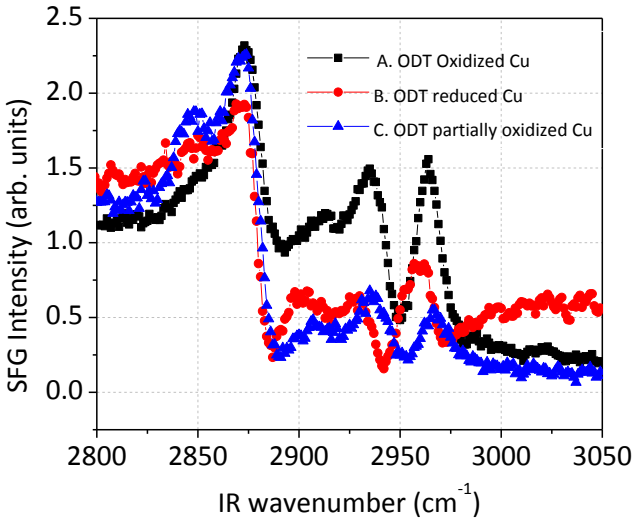

Figure 4.4 SFG spectrum of ODT on Cu, A: oxidized, B: reduced, C: partially oxidized.

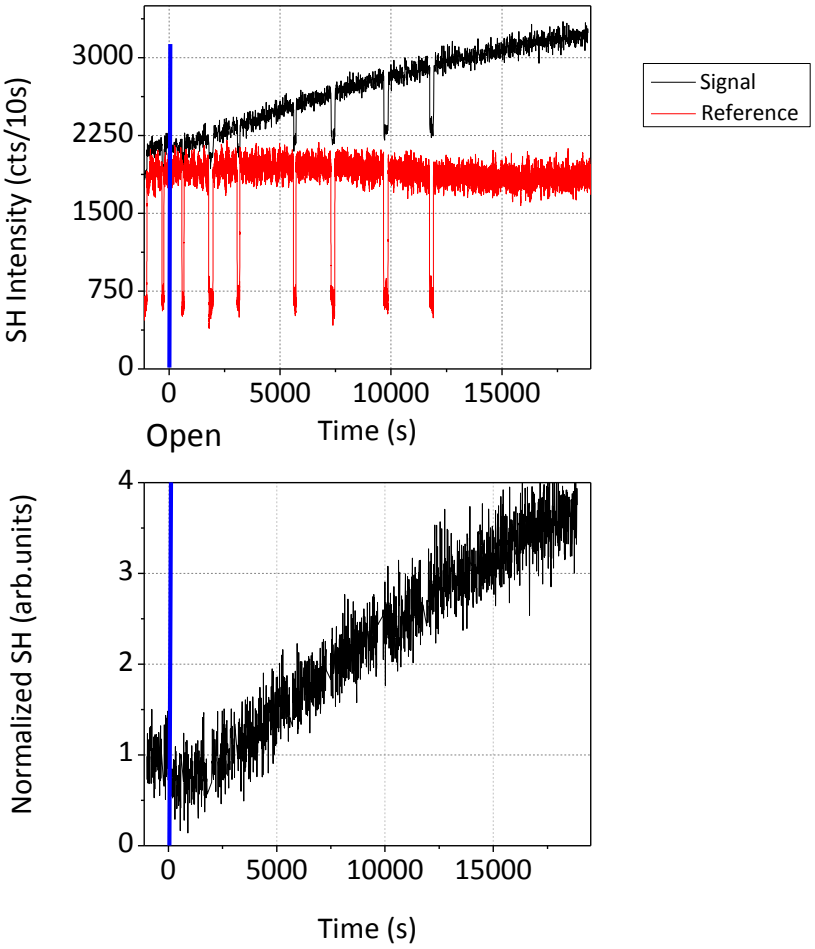

Figure 4.5 Top: Raw Data of Cu-ODT exposed to humid air.

Bottom: Background subtracted SHG of Cu-ODT exposed to humid air.

The oxidation kinetics are monitored for the partially oxidized substrate, and qualitatively, the signal initially shows a slight fast decrease before increasing for the next 17000 s and reaching a plateau. Whenever Cu is partially oxidized, the SH signal can still grow due to formation of an oxide layer. Qualitatively, the signal takes much longer to plateau. The final set of data corresponds to ODT bound to a reduced Cu substrate. This is shown in **Figure 4.6**. Of note, the signal is very weak. This is a

combination of two effects. First, when ODT is bound to the surface, previous SHG studies[46] have shown that at monolayer coverage, the signal is at a minimum. Also, by observing the SHG kinetic data corresponding to the dry sample, the SHG signal tends towards a minimum as the first monolayer is formed.

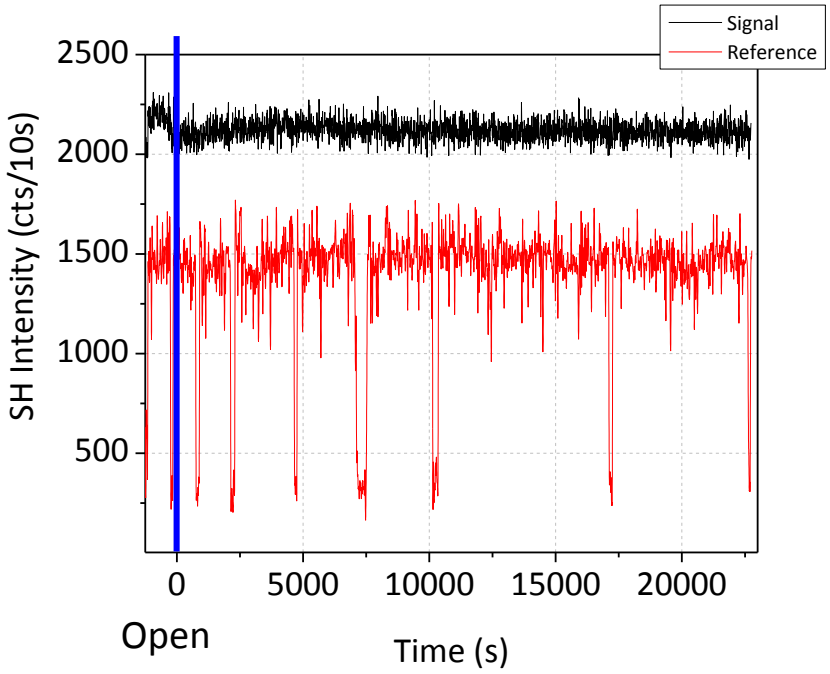

Figure 4.6 Raw Data showing the SHG response of ODT bound to a reduced Cu substrate.

iii. Discussion

When Cu is exposed to dry air, the apparent signal decrease in the SHG may be attributed to an initial loss in free electron density at the surface, and this result is comparable to early studies done on metallic substrates by Shen.[6,7] **Figure 1.3** and **Figure 2.2** illustrated this for the case of O_2 and CO adsorbing onto metallic

substrates. It is generally accepted that the chemisorption bond decreases the free electron density of the metallic substrate correspondingly leading to a decrease in SHG intensity.[6,9] Thus, qualitatively, during the first 3000 seconds of the SHG measurement under dry air, O_2 chemisorbs to the metallic surface forming the first monolayer of oxide film. After the chemisorption is complete, the growth of a second monolayer of Cu_2O gives the dominant contribution to the SHG signal due to an electronically resonant contribution due to bandgap (2.1 eV) excitation of Cu_2O.[24] This case differs markedly from the SHG observed from the bare metallic substrate exposed to humid air.

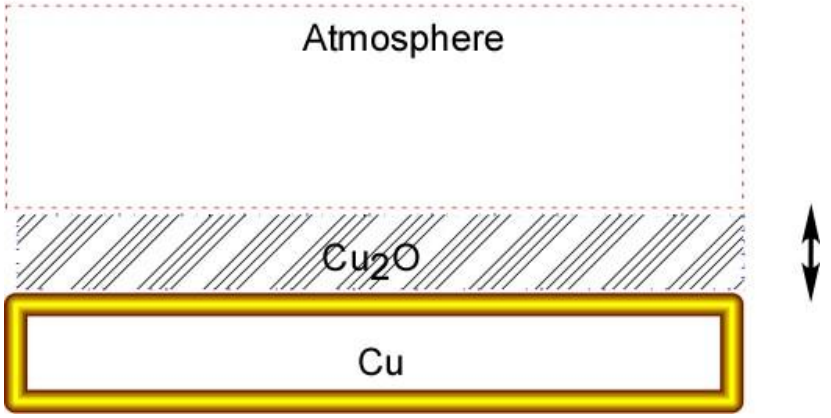

Figure 4.6 Schematic illustration of oxide film growth on dry Cu. SHG monitors chemisorption onto the substrate and subsequently oxide film growth, until the surface is seen to saturate.

As shown by IRAS and QCM,[1,3,4] the SHG measurements under humid conditions also demonstrate that Cu_2O formation is very sensitive to the physisorbed aqueous adlayer. Upon initial exposure of the Cu to air, no chemisorption sequence is observed; the signal immediately jumps to 1.8 times the signal from the bare substrate indicating that the oxide film growth is rapidly accelerated by the presence of water. The signal continues to grow, until a peak is reached, and the SHG signal is then observed to slightly decrease. Unfortunately, this measurement was not carried out for a longer period of time. Possible oscillations in SHG signal may occur as the Cu_2O film forms layer by layer as SFG studies have shown for film growth on single crystal surfaces.[47,48]

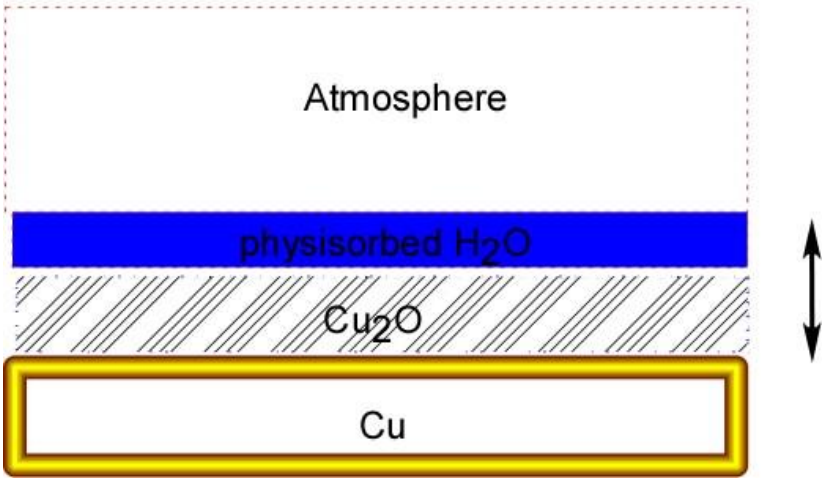

Figure 4.7 Schematic illustration of oxide film growth in the presence of an aqueous adlayer. SHG indicates that oxide film growth is accelerated and possible layer by layer growth can be observed in situ.

Upon comparison to **Figure 1.4**, the SFG spectrum in **Figure 4.4** indicates the presence of a small oxide film of the Cu substrate coated with ODT. After initial observation with SFG, the sample's oxidation kinetics were monitored with SHG. At the onset of exposure, chemisorption onto the substrate is still possible observed because of the small initial decrease in SHG. Oxide monolayer growth starts to dominate the signal as the SHG signal is observed to rise until possible saturation after 17000 s of exposure.

Whenever ODT is bound to a reduced Cu sample, data in **Figure 4.5** suggest that ODT serves to hinder formation of the oxide. Initially, the signal from the substrate coated with ODT is very weak, and upon exposure to humid air, the signal from the sample decreases and does not recover. Upon comparison to **Figure 4.1** and **Figure 4.2**, monolayer formation of the oxide is thought to occur. For this particular experiment, a better signal to noise ratio would be advantageous.

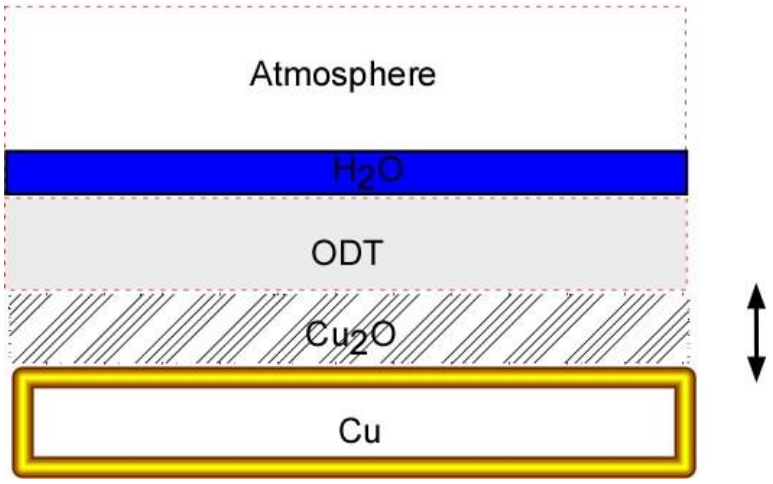

Figure 4.8 In the presence of ODT, oxide film growth is observed to slow under humid conditions when compared to dry copper. The signal is observed to saturate predicting that oxide formation is slowed by the presence of ODT.

iv. Summary and Conclusions

SHG has been used to monitor the O_2 chemisorption and subsequent Cu_2O formation on a metallic Cu substrate. Humidity is shown to have a marked effect on the SHG response from a polished bulk copper sample. The chemisorption step is not resolvable under the current experimental conditions, and Cu_2O film formation immediately begins to occur upon exposure to humid air. Adding ODT to the surface decreases the rate of Cu_2O film formation when compared to the bare metallic substrate. SHG acts as a valuable and complimentary in situ probe to SFG to monitor changes in the vibrationally nonresonant signal from the metallic substrate.

A set of further experiments could be performed under controlled conditions to help cement conclusions drawn from this work. First, a background signal could be taken with the sample under N_2 gas. Next the cell can be evacuated, and at time zero, a gas could be introduced into the cell. A future experiment could involve the use of pure O_2 gas to monitor the adsorption kinetics. To further this work, the effect of a stream of pure water vapor could be analyzed on the bare metallic substrate. A mixture of reactive gases could also be exposed to the sample, and under these conditions oxide formation would proceed at faster rates. Another experiment may also be performed with an atomically clean sample exposed to O_2 at ambient pressure.

The heterogeneity of the polished sample might perturb the overall oxidation effects, so some of the models presented may not be close to a microscopic physical reality. Cuprous oxide may not be the only species formed at the interface as cited in previous work by Persson and Leygraf.[4] Ex situ probes such as XPS or cathodic reduction could also be added to provide some quantitative results and estimate the oxide thickness.

References

(1) Leygraf, C.; Marcel Dekker: New York, 1995, p 426.
(2) Thiel, P. A.; Madey, T. E. *Surface Science Reports* **1987**, *7*, 211.
(3) Aastrup, T.; Wadsak, M.; Schreiner, M.; Leygraf, C. *Corrosion Science* **2000**, *42*, 957.
(4) Persson, D., Leygraf, C., *J. Electrochem. Soc.* **1993**, *140*, 1256.
(5) Aastrup, T.; Leygraf, C. *Journal of The Electrochemical Society* **1997**, *144*, 2986.
(6) Tom, H. W. K.; Mate, C. M.; Zhu, X. D.; Crowell, J. E.; Heinz, T. F.; Somorjai, G. A.; Shen, Y. R. *Physical Review Letters* **1984**, *52*, 348.
(7) Zhu, X. D.; Shen, Y. R.; Carr, R. *Surface Science* **1985**, *163*, 114.
(8) Heinz, T. F., University of California, 1982.
(9) Richmond, G. L.; Robinson, J. M.; Shannon, V. L. *Progress in Surface Science* **1988**, *28*, 1.
(10) Grubb, S. G.; DeSantolo, A. M.; Hall, R. B. *The Journal of Physical Chemistry* **1988**, *92*, 1419.
(11) Ishida, H.; Mizoguchi, R.; Onda, K.; Hirose, C.; Kano, S. S.; Wada, A. *Surface Science* **2003**, *526*, 201.
(12) Higgins, D. A.; Abrams, M. B.; Byerly, S. K.; Corn, R. M. *Langmuir* **1992**, *8*, 1994.
(13) Eisenthal, K. B. *Accounts of Chemical Research* **1993**, *26*, 636.
(14) Eisenthal, K. B. *Chemical Reviews* **1996**, *96*, 1343.
(15) Benderskii, A. V.; Eisenthal, K. B. *The Journal of Physical Chemistry B* **2001**, *105*, 6698.
(16) Liu, Y.; Dadap, J. I.; Zimdars, D.; Eisenthal, K. B. *The Journal of Physical Chemistry B* **1999**, *103*, 2480.
(17) Dadap, J. I. *Physical Review B* **2008**, *78*, 205322.
(18) Dadap, J. I.; Shan, J.; Heinz, T. F. *J. Opt. Soc. Am. B* **2004**, *21*, 1328.
(19) Shan, J.; Dadap, J. I.; Stiopkin, I.; Reider, G. A.; Heinz, T. F. *Physical Review A* **2006**, *73*, 023819.
(20) de Beer, A. G. F.; Roke, S.; Dadap, J. I. *J. Opt. Soc. Am. B* **2011**, *28*, 1374.
(21) Shen, Y. R. *Annual Review of Materials Science* **1986**, *16*, 69.
(22) Corn, R. M.; Higgins, D. A. *Chemical Reviews* **1994**, *94*, 107.
(23) Lantz, J. M.; Corn, R. M. *The Journal of Physical Chemistry* **1994**, *98*, 4899.
(24) Baten, S. M. A.; Taylor, A. G.; Paul Wilde, C. *Electrochemistry Communications* **2007**, *9*, 2393.
(25) Yan, E. C. Y.; Liu, Y.; Eisenthal, K. B. *The Journal of Physical Chemistry B* **1998**, *102*, 6331.

(26) Wang, H.; Yan, E. C. Y.; Borguet, E.; Eisenthal, K. B. *Chemical Physics Letters* **1996**, *259*, 15.
(27) Eisenthal, K. B. *Chemical Reviews* **2006**, *106*, 1462.
(28) Rao, Y.; Hong, S.-Y.; Turro, N. J.; Eisenthal, K. B. *The Journal of Physical Chemistry C* **2011**,*115*, 11678.
(29) Laibinis, P. E.; Whitesides, G. M. *Journal of the American Chemical Society* **1992**, *114*, 9022.
(30) Hosseinpour, S.; Hedberg, J.; Baldelli, S.; Leygraf, C.; Johnson, M. *The Journal of Physical Chemistry C* **2011**, *115*, 23871.
(31) Chen, C. K.; Heinz, T. F.; Ricard, D.; Shen, Y. R. *Physical Review Letters* **1981**, *46*, 1010.
(32) Guyot-Sionnest, P.; Chen, W.; Shen, Y. R. *Physical Review B* **1986**, *33*, 8254.
(33) Bloembergen, N.; Pershan, P. S. *Physical Review* **1962**, *128*, 606.
(34) Franken, P. A.; Hill, A. E.; Peters, C. W.; Weinreich, G. *Physical Review Letters* **1961**, *7*, 118.
(35) Guyot-Sionnest, P.; Shen, Y. R. *Physical Review B* **1988**, *38*, 7985.
(36) Guyot-Sionnest, P.; Shen, Y. R. *Physical Review B* **1987**, *35*, 4420.
(37) Zimdars, D.; Eisenthal, K. B. *The Journal of Physical Chemistry A* **1999**, *103*, 10567.
(38) McGlip, J. F.; Yeh, Y. *Solid State Communications* **1986**, *59*, 91.
(39) DeLong, K. W.; Trebino, R.; Hunter, J.; White, W. E. *J. Opt. Soc. Am. B* **1994**, *11*, 2206.
(40) Yamada, C.; Kimura, T. *Physical Review B* **1994**, *49*, 14372.
(41) Stehlin, T.; Feller, M.; Guyot-Sionnest, P.; Shen, Y. R. *Opt. Lett.* **1988**, *13*, 389.
(42) Armstrong, S. R.; Hoare, R. D.; Pemble, M. E.; Povey, I. M.; Stafford, A.; Taylor, A. G. *Journal of Crystal Growth* **1992**, *120*, 94.
(43) Ducuing, J.; Bloembergen, N. *Physical Review Letters* **1963**, *10*, 474.
(44) Rivera-Rubero, S.; Baldelli, S. *The Journal of Physical Chemistry B* **2004**, *108*, 15133.
(45) Jacob, J. D. C.; Rittikulsittichai, S.; Lee, T. R.; Baldelli, S. *The Journal of Physical Chemistry C* **2013**, *117*, 9355.
(46) Buck, M., Eisert, F. Fischer, J., Grunze, M., Trager, F. *Applied Physics A* **1991**, *53*, 552.
(47) Hirose, C.; Ishida, H.; Iwatsu, K.; Watanabe, N.; Kubota, J.; Wada, A.; Domen, K. *The Journal of Chemical Physics* **1998**, *108*, 5948.
(48) Ishida, H.; Iwatsu, K.; Kubota, J.; Wada, A.; Domen, K.; Hirose, C. *The Journal of Chemical Physics* **1998**, *108*, 5957.